Numerical analysis and parametric study of unreinforced masonry walls with arch openings under lateral in-plane loading

3 authors, including:

Milon Kanti Howlader
University of Newcastle
18 PUBLICATIONS **69** CITATIONS

M. C. Griffith
University of Adelaide
216 PUBLICATIONS **3,636** CITATIONS

Some of the authors of this publication are also working on these related projects:

Project   Assessment of Heritage Stone and Brick Masonry Buildings Under Earthquake Actions View project

Project   Simulation of Heritage Structures View project

Numerical Analysis and Parametric Study of Unreinforced Masonry Walls with Arch Openings under Lateral In-Plane Loading

M. K. Howlader[1*]; M. J. Masia[2] and M. C. Griffith[3]

[1*]PhD Student, Centre for Infrastructure Performance and Reliability, The University of Newcastle, Callaghan NSW 2308, Australia, MilonKanti.Howlader@uon.edu.au (corresponding author)

[2]Associate Professor, Centre for Infrastructure Performance and Reliability, The University of Newcastle, Callaghan, NSW 2308, Australia, mark.masia@newcastle.edu.au

[3]Professor, School of Civil, Environmental and Mining Engineering, The University of Adelaide, North Terrace Campus, SA 5005 Australia, michael.griffith@adelaide.edu.au

Abstract

This paper presents numerical modelling of the in-plane shear behaviour of unreinforced masonry (URM) walls with a semicircular arch opening. To do so, two dimensional finite element (FE) modelling of a series of experimentally tested walls was conducted using the simplified micro-modelling approach. The models successfully captured the load-displacement behaviour and, to a large extent, the failure modes of the piers and spandrels observed in the experimentally tested walls. The exception was that the FE modelling did not show pier diagonal shear cracking which was observed in some of the tested walls. The model was then used to perform parametric studies to investigate the effect of geometric variations of the walls as well as the effect of vertical pre-compression stresses on the lateral in-plane capacity of the walls. The results obtained from the FE analyses were compared to the anticipated maximum shear strength and the predicted failure modes according to the New Zealand Society for Earthquake Engineering (NZSEE) [22]. From this study, it is shown that there is a significant effect of the wall geometry and vertical pre-compression load on the failure modes and the lateral load resistance capacity of the walls. In most of the cases investigated, the NZSEE equations for maximum shear strength and failure modes agree well with the FEM results. The arch opening was remodelled to a rectangular opening and it was found that the effective pier height for an equivalent rectangular pier adjacent to a semi-circular arched opening can be taken up to the half height of the arch radius.

Keywords: Unreinforced masonry, in-plane lateral loading, FEM, aspect ratio, pre-compression load, wall openings, piers, spandrels

1. Introduction

Unreinforced masonry (URM) structures, particularly those which were designed and constructed prior to the introduction of modern seismic design codes, are vulnerable to damage when subjected to strong ground motion during earthquakes. This vulnerability arises because such structures have high mass and stiffness and hence attract high forces during earthquakes, combined with low tensile strength and ductility to resist such forces. Due to the significant nonlinear behaviour and orthotropy of URM structures, it is difficult for design engineers to evaluate the load displacement and vulnerability analyses of such structures. At low levels of load, masonry acts as a linear elastic material and at high levels of load it behaves as non-linear material [1]. The non-linear behaviour of the masonry is mostly concentrated in the joints between the masonry units [2,3] and hence the most complex part of the modelling is to model the behaviour of the joints in the masonry.

Masonry walls may suffer damage and potential collapse when subjected to ground shaking acting normal (out-of-plane) to the wall or parallel (in-plane) to the wall. The current study considers walls subjected to gravity loading combined with in-plane lateral loading. In particular, the current study considers walls with window or door openings as such walls typically represent the weak link in the lateral load resisting system for URM buildings. To investigate the in-plane behaviour of URM walls, researchers [4-10] have performed in-situ and laboratory testing of URM structures in full or reduced scales. Experimental testing is time consuming and costly and in most cases, it is challenging to obtain the permission to collect samples or to set-up instrumentation in field sites. These challenges motivated researchers to perform computer aided numerical modelling to predict the vulnerability of URM structures considering the nonlinear material behaviour of the masonry.

Various authors have carried out numerical analyses to predict the in-plane behaviour of masonry walls using different modelling strategies. Equivalent frame (EF) modelling [11-14] was conducted by dividing a wall with window or door openings into a group of deformable panels (piers and spandrels) represented using beam elements and connecting them with rigid joints, where nonlinearity of the panels was captured by using the nonlinear constitutive material model. In the macro-element approach, the piers and spandrels were modelled using the macro-element [15] instead of beam elements as used in the EF modelling. Both of the above mentioned modelling strategies are suitable for simple and regular wall configurations to predict the load resistance capacity of the wall. Despite the ability to extract valuable information, the models are necessarily simplified (for computational efficiency) and do not consider the multifaceted nature of the masonry.

Macro-modelling and micro-modelling finite element modelling approaches of masonry structures which consider the nonlinearity of the masonry were proposed [3, 16] and have become popular among masonry researchers [17-

20]. Of the two approaches, the micro-modelling approach is more detailed where the interaction between the units and the joints are considered explicitly using interface elements. On the other-hand, in the macro-modelling approach the masonry is considered as homogeneous continuum material without distinguishing the individual units and joints.

In the current study, a simplified micro-modelling FEA approach was adopted using the commercially available finite element (FE) software DIANA 10.2 [21]. The nonlinear behaviour was taken into consideration to represent the complex nature of the URM wall including the potential for shear cracking and/or sliding and rocking and/or toe crushing. This paper consists of two parts. In the first part, the FE model was verified against experimental data obtained by the authors with respect to the in-plane load versus displacement behaviour and failure modes. Then in the second part, the validated model was used to evaluate the effect on wall behaviour of the aspect ratios (height to length) of piers and spandrel, and the imposed vertical pre-compression stress on the piers. The FEA results were compared to the predictions made using NZSEE [22]. In addition to this, the arched opening was modelled also as a rectangular opening to define the effective rectangular pier height in the case of semi-circular arched openings in URM walls. Finally, the masonry prism compression test was also modelled to investigate and compare variations observed between model and experimentally observed specimen stiffnesses.

2. Experimental Testing Program

Eight full-scale perforated URM walls were subjected to constant vertical load representing gravity loading combined with cyclic in-plane lateral displacements using the test setup shown in Fig. 1.

The testing program was carried out in the structural engineering laboratory at The University of Newcastle, Australia and considered three different wall geometries (Fig. 2), with all walls being two wythes (230 mm) thick solid construction, using common bond with a course of header units at every fourth course. Seven of the eight walls had the same overall length and height but with variations in the pier and spandrel aspect ratios achieved by varying the depth of the spandrel (Figs. 2a and 2b). The eighth wall was constructed with asymmetric pier lengths by increasing the length of one of the piers (Fig. 2c). The walls were designed to represent a single storey section of wall from a larger building façade typical of heritage URM buildings in Australia. All the walls were constructed with the same type of solid clay brick (nominal dimensions: 230 mm long, 110 mm wide and 76 mm high) and the same mortar mix ratio of 1:2:9 (cement: lime: sand) by volume. The walls were constructed in- situ in the testing location directly on a reinforced concrete footing beam. The footing beam was fixed to the laboratory strong floor. The bottom course of masonry was prevented from sliding relative to the footing beam via the use

of steel struts placed on either side of each pier (Fig. 1), but was not prevented from uplifting. The boundary condition along the upper edge of the wall allowed in-plane rotation of the pier-spandrel sub-assembly and the loading beam arrangement was in contact with the wall only along the length of each pier. The resulting gap provided immediately above the spandrel was designed to represent the presence of another opening above the spandrel in a multi-storey building façade. This allowed unrestrained vertical deformation of the spandrel along its top edge.

The testing protocol involved first applying the vertical loading to a predetermined level, which was held constant during testing. The in-plane lateral displacement was then applied in increasing reversing cycles as shown in Fig. 3 (0.5(0.01) denotes 0.5 mm displacement applied at a rate of 0.01 mm/sec). The displacement was increased until a post-peak reduction in the in-plane lateral load exceeding 20% of the peak lateral load was achieved, or until 2% drift, if a 20% reduction was not achieved. The level of vertical pre-compression imposed on the walls was varied to represent walls at different locations in a multi-storey building and for three of the combinations of geometry and pre-compression level, two theoretically identical specimens were tested. Further details regarding the experimental testing program can be found in [23].

3. Numerical Modelling

The tested walls (Fig. 2) were modelled using the commercial software package Diana 10.2 [21]. The micro-modelling strategy adopted, including detailed descriptions of the geometric and material input properties, together with the sources of the material data, and model validation against the experimental testing results, are described here. In selecting a suitable modelling strategy, the authors conducted both simplified micro-modelling and macro-modelling of the wall tests [42]. It was found that the macro-modelling approach resulted in a close agreement with the micro-modelling for initial stiffness, but over-predicted peak loads compared to the micro-modelling strategy. In addition, the macro-modelling failed to correctly capture post peak softening which was observed in the experimental program and was successfully captured by the micro-modelling strategy. Based on this comparison [42], the micro-modelling strategy was selected and is presented in the current paper because it is able to discretely capture cracking in the wall and was found to more accurately match the behaviour observed in the testing program.

3.1 Wall Model

A two dimensional simplified micro-modelling approach was used to model the masonry walls. In this approach, the brick units were modelled using continuum elements and the mortar joints, brick/mortar interface and potential

brick cracks were modelled using interface elements. Four-noded quadratic (Q8MEM) rectangular isoparametric linear plane stress elements with thickness equal to the wall thickness of 230 mm were used to model the solid brick units. The mortar joint and the potential brick crack interfaces were modelled with four-noded (L8IF) linear interface elements. As the mortar joints and the mortar/brick unit interface were lumped together into zero thickness interface elements, the brick units were expanded both in height and length to keep the overall geometry of the wall consistent with the real masonry.

Interface elements were used at each quarter length of the brick to model the potential crack planes through the brick. In previous FE micro-modelling by the authors the potential brick cracks were modelled using an interface only at the mid-length of each brick [19, 21, 24-25]. However, due to the use of the common bond pattern in the walls for the current study, the header courses were placed in every fourth course as shown in Fig. 4(a). To construct the header courses, the vertical joints are offset from the stretcher courses above and below by one quarter brick length, otherwise the vertical mortar joints would align over three adjacent courses, thus reducing integrity of the wall. Hence, considering the resulting masonry assemblage and to match properly with the nodes of the surrounding elements in the finite element model, potential crack surfaces (interface elements) at each quarter length of the brick was deemed appropriate. Although the interface elements have zero thickness, for illustrative purposes a fake thickness of 5 mm is used to highlight the interface locations in the model (Fig. 4 (b)). Each quarter brick section was divided into two elements across its length and two elements across its height. To match the meshing division of the brick units with the surrounded interface elements, two interface elements were used across each quarter brick length and each brick height. Hence, full bricks were made with sixteen continuum plane stress elements and six brick crack interface elements. Along each brick length eight mortar joint interface elements existed. The brick unit elements behave linear elastically and all of the nonlinear behaviour was modelled through the interface elements.

The combined crack-shear-crush interface model which is incorporated in DIANA 10.2 [21], developed and validated by [26, 27], was used to model the mortar joint interface elements. The crack-shear-crush model is based on the multi-surface plasticity, which involves the tension cut-off model to describe the joint cracking failure, Coulomb-friction model to depict the sliding shear failure and the elliptical cap model to explain the masonry compression as well as the diagonal cracking of the brick unit. The normal uplift upon the shear-sliding behaviour (known as the dilatancy of the masonry joint) developed by [27] is also encompassed in the composite interface material model.

For the potential brick crack, a simple tension softening model is used, which is similar to the tension cut-off model used in the mortar joint interface model. The only difference is that here the tension softening occurs linearly instead of the exponential softening curve used in the mortar joint model. After the initiation of cracking, it is assumed that the shear stress drops immediately to zero and hence this interface model does not include the shear and compression failure criterion. To ensure the continuity of the brick displacement through the interface, a high stiffness value is chosen which also confirms the impossibility of the frictional sliding of the brick along the potential crack surface.

In this wall modelling technique, at first a quarter brick with the interface elements representing the brick crack and the mortar joint were created. All the physical and material properties are set in the quarter brick and the interface brick crack and mortar joint elements. Then by copying the elements and doing some modifications (especially in the arched portion where the bricks and the interface elements are modelled one by one), the final brick wall models (Fig. 5 represents the deep spandrel wall) were prepared to the required geometry, which represent the experimentally tested walls. The thickness of the elements both used for plane stress and line interface are taken as 230 mm which is equal to the thickness of the walls.

For the steel sections representing the upper boundary conditions imposed on the walls during testing, four-noded quadratic (Q8MEM) rectangular plane stress elements were used. The height of the steel sections in the FE model were kept the same as those used in the testing program to maintain the correct location of the vertical and horizontal loading. To achieve the correct stiffnesses for the steel sections, the thicknesses of the elements were calculated to achieve the equivalent second moment of area for each steel section. Hence the element thicknesses of the composite steel section just above the pier length of 162 mm and for the steel I section (200UC 46.2) of 65.84 mm were given as geometric property inputs in the model. In Fig. 5 F_y and d_x denote the vertical load and horizontal displacement respectively. To simulate the fixed boundary condition at the bottom of the wall, all the nodes along the base of the walls were restrained against translation in both x and y directions.

Three load cases were applied in the model, which were self weight of the wall (W), pre-compression load (F_y) and horizontal deformation (d_x). The self weight (W) and the vertical precompression loads (F_y) were applied once and kept constant in a single step. Horizontal displacement (d_x) was then applied monotonically at the centre of the loading beam with 600 steps by increasing with constant step size of 0.08 mm up to a maximum of 48 mm deflection or when 20% post peak lateral load drop occurred.

3.2 Material Properties

The material properties used as input parameters in modelling were obtained from material characterisation testing conducted in parallel with the wall testing program. The masonry prism compression test [28, 29], triplet shear test [30] and the bond wrench test [31] were conducted to define the material properties in the mortar joint interface elements. Modulus of rupture test [32] was used to define the tensile strength of the potential brick crack interface elements. The bond wrench test was used to measure the flexural tensile strength of the brick to mortar bond. Similarly, the modulus of rupture test was used to measure the flexural tensile strength of the bricks. The direct tensile strengths were then obtained by dividing the flexural tensile strengths by 1.5 based on the findings of [41]. Tensile fracture energy was not measured directly, but rather correlated to tensile strength for the mortar joints and brick following the recommendations of [34] and [33] respectively. In the prism compression tests, LVDTs were placed across gauge lengths representing the mortar joints and the masonry (3 units and 3 joints), from which Young's Moduli for the joints and masonry were determined. Young's Modulus for the brick material (E_b) was then determined from compatibility considerations. Some other required parameters were taken from the literature. All masonry material testing, except for bond wrench testing, was conducted at an age of approximately 28 days which matched the age at testing of all wall specimens except for the first wall tested (which was tested at age 5 months). Bond wrench testing was conducted for each mortar batch mixed during the whole testing program at the same age as the wall test for the wall using that mortar. The input material properties used in the FE model, together with the data sources are presented in Table 1.

3.3   Validation of Model against Experimental Test Results

3.3.1   Load-displacement response

The lateral load-displacement envelop curves for the experimentally tested walls (positive and negative displacement directions) are compared to the simulated force-displacement relationships obtained from the FEA in Fig. 6. In the specimen naming convention shown in Fig. 6, WS stands for shallow spandrel wall geometry (Fig. 2a) and WD for deep spandrel geometry (Fig. 2b). The number (0.2 or 0.5) indicates the average vertical pre-compression stress (0.2 MPa or 0.5 MPa) imposed on the piers. In the case of the asymmetric pier specimen WD_0.4/0.7 (Fig. 2c), the specimen had a deep spandrel and piers of different lengths resulting in different average stress in each pier. The longer pier had an average pre-compression stress of 0.4 MPa and the shorter, 0.7 MPa. For the three geometry / pre-compression scenarios for which two tests were conducted, the letters A or B differentiate between the two theoretically identical specimens. Due to the symmetric geometry for seven of the eight tested walls, the load-displacement behaviour for FEA was simulated in one direction only and then assumed the same in both positive and negative directions for comparison with the experimental load-displacement plots.

In the case of wall WD_0.4/0.7, the FEA was carried out by imposing the lateral displacement in each direction separately due to the asymmetric geometry. Hence, in Fig. 6(e), the FEA pushover curves in positive and negative directions are different.

The FEA results are generally in good agreement with the experimental results showing extensive nonlinearity after the initial linear portion. In all the cases, the FEA results over estimate the maximum lateral loads observed in the experiments, which may result from the FEA simulating a monotonic application of displacement, compared to the cyclic displacement applied in the experimental program. However, the difference in the peak load values between model and test was less than 15% considering all the walls. The FEA results showed higher initial stiffness than the experimental results in all cases. In the case of wall WS_0.2_A, the FEA result was closer to the experimentally observed initial stiffness than for WS_0.2_B. As the wall WS_0.2_A was tested after 5 months from the construction date, it is expected that the lime rich mortar was not able to gain its full strength (and stiffness) after 28 days (the other walls were tested at nearly 28 days).

For WS_0.2 (Fig. 6a), the post peak drop in lateral load equal to 20% of the maximum load was not achieved in the FEA or in either of the tested walls prior to reaching a displacement of 48 mm (2% drift). However, the post peak load drop trend was slightly greater in the FEA than in the experiments.

In the other cases, the targeted 20% load drop was achieved in the FEA before reaching 48.0 mm displacement. By comparison in the experimental wall tests, the 20% load drop occurred in WS_0.5 and WD_0.2 in either one direction or both directions during testing of at least one of the two specimens if two specimens were tested. However, there were cases, such as WS_0.5_A and WD_0.5_B, which were taken to 2% drift without experiencing a 20% post peak drop in load. In case of wall WD_0.5_A and WD_0.4/0.7, the load drops were not 20% at ultimate displacement, but the tests were stopped at 24.0 mm displacement due to excessive diagonal shear damage of the piers. The experimental maximum lateral load values for the walls presented in

Table 2 were obtained by averaging the maximum values in push and pull directions (average of four values in the case of repeated walls).

3.3.2   Failure modes

The crack patterns observed in the tested walls at the ultimate limit state are presented together with the FEA predicted failure modes in Fig. 7-Fig. 11 . Fig. 7 to Fig. 10 show only the damage patterns for push (+) cycles for comparison with the FEA predictions. However, in case of the asymmetric wall (WD_0.4/0.7), both push and pull direction crack patterns are presented to compare with the separate FEA simulations in each direction (Fig. 11). The crack patterns for the tested walls are presented by plotting the contour map of the major principal strain

obtained from digital image correlation (DIC) analysis. In the case of FEA, the failure mode is visualised by the contour map of the crack strain perpendicular to the interface.

In the experimental testing program, the failure of the piers included examples of both pier rocking and/or toe crushing (flexural failure modes) and diagonal shear failure. The flexural failure occurred at the lower pre-compression level and both shear and flexural failures occurred in the case of the higher pre-compression level. However, in the FEA, the failure of the piers were flexural in all cases. In the case of spandrel failure, there was mixed shear and flexural failure in both the tested walls and FEA simulations (despite this not showing clearly in Fig. 7(c) and Fig. 9(b) due to the scale of the contour plot). With the increase of pre-compression level, the spandrel cracking was more prominent, both in the tested walls and the FEA simulations. Cracking along the upper most mortar layer throughout the wall length was shown in both test and FEA. Noticeable damage of the mortar joints in the joint region between piers and spandrels, as well as spandrel movement over the opening was also visible in the case of the higher pre-compression level. Prominent diagonal shear cracking through the spandrel was observed in the case of deep spandrel walls with higher pre-compression.

The failure of the FEA model to predict diagonal shear cracking in the piers for the walls tested in the current study is not considered to represent a failing of the model. It should be considered that in both the cases of WS_0.5 and WD_0.5, one of two repeat specimens for each of these geometry / pre-compression scenarios displayed diagonal shear cracking while the other theoretically identical specimen did not. It may be concluded that variations in material properties between repeat specimens may have triggered one failure mode over the other and the FEA model successfully predicted one of the two alternative failures. It should also be considered that progressive damage due to reverse cyclic displacements in the tested walls may result in some differences in the final failure patterns compared to the monotonic application of displacement as applied in the FEA.

Based on the above observations and comparisons it was concluded that the FEA model captured successfully the key features of damage and failure modes observed experimentally.

4. Parametric Study

Using the validated FEA wall model, the influence of aspect ratio of the piers and spandrel and the imposed pre-compression stresses on the in-plane behaviour of the URM walls were investigated. The material properties were kept constant for all models as shown in Table 1. The specimens simulated for the parametric study are designated according to the geometric and loading configurations. For example, P2.04_S0.72_0.2 refers to a specimen with pier aspect ratio 2.04, spandrel aspect ratio 0.72 and the imposed pre-compression stress on each pier of 0.2 MPa. In defining pier and spandrel aspect ratios in the presence of a semi-circular arched opening, the depth of the

spandrel was taken as the depth measured to one-third of the arch radius below the top of the arch [22]. Hence, the pier height was taken by extending the straight portion of the pier by two-thirds of the arch radius.

4.1 Geometric Variations

To assess the effect of wall geometry, aspect ratios of the piers and spandrel were varied resulting in a total of six geometric configurations (Fig. 12). Pier aspect ratio (height / length) was varied from 2.04 to 0.85 and spandrel aspect ratio (depth / length) was varied from 1.07 to 0.72. The opening width and the arch configuration were kept the same for all simulations and the different aspect ratios were achieved by varying the pier height and length and the spandrel depth. These aspect ratios result in the pier being considered squat to slender and the spandrel deep to shallow as defined [37]. The bonding pattern of the masonry was common bond, where header courses were used at every forth course, as was used in the experimental program. It is noted that geometries P2.04_S0.72 and P1.63_S1.07 are in fact the same as the experimentally tested geometries WS and WD.

4.2 Variation of Pre-compression Stress

As observed in the experimental program, the lateral load capacity and the failure mode of URM walls vary with the pre-compression stresses. The pre-compression level on a wall can vary due to its position within a building. Observations from previous earthquakes have found that the nature of failure of in-plane loaded walls is diverse in different levels of the same building. Australian URM buildings are mostly low-rise structures [38], so 0.5 MPa is a high pre-compression level in the Australian context. However, in Europe, according to the research report of [39], researchers have performed experimental programs for higher pre-compression stresses to determine the in-plane behaviour of walls. Hence, for the current parametric study pre-compression stress values of 0.2 MPa, 0.5 MPa, 0.7 MPa and 1.0 MPa were applied which are equal to 2.8%, 7.1%, 10% and 14.3% of the experimentally measured masonry compressive strength respectively.

4.3 Results from the Parametric Study

The load-displacement plots are grouped for each of the six different geometries in Fig. 13 with each figure showing the plots for the four pre-compression levels simulated. The reported displacement is the displacement applied at the mid length of the loading beam (d_x in Fig. 5). It can be seen in Fig. 13 that with the increase of the pre-compression level, the lateral load capacity increases for all geometric configurations. Also, for low pre-compression level and slender piers, there is no significant load drop at 24 mm (i.e. 1% drift) displacement. But with the increase of the pre-compression level and for more squat piers, the post peak load drop is more prominent and the ultimate state (post peak load drop equal to 20% of the maximum load) occurred before reaching the simulated 24 mm displacement.

Alternatively, Fig. 14 presents the maximum lateral load resistance (V_{max}) for each of the six geometries, grouped for each of the pre-compression levels. With the decrease of the pier aspect ratio, the lateral load capacity increases and this load increase is notable at 1.26 pier aspect ratio and below. It should be noted that for pier aspect ratios 1.26 and lower the total pier cross sectional area is also increasing, making direct comparison difficult. However, for the three wall geometries shown in Fig. 12 a, b, c (pier aspect ratios 2.04, 1.84, 1.63 respectively) the cross sectional areas of the piers and wall heights are unchanged allowing the effect of pier aspect ratio to be isolated. Fig. 14 shows that the increase in lateral load capacity with decreasing pier aspect ratio across this range is minimal indicating that lateral load capacity is relatively insensitive to pier aspect ratio. Therefore, the increase in load capacity for the pier aspect ratios of 1.26, 0.94 and 0.85 is more likely related to the increase in pier cross sectional area and/or reduction in wall height for these geometries.

Finally, bi-linear idealisations of the FEA pushover curves were obtained according to [40] as described in Fig. 15. In this method, the elastic stiffness, k_{el} is measured by the ratio of lateral load at $0.70V_{max}$ (assumed first crack load = V_{cr}) and its corresponding displacement. The ultimate displacement δ_u is taken as the value of d_x at which the lateral load V has dropped (post peak) by 20% of the peak load, or the maximum simulated displacement of 24 mm if a 20% load drop was not experienced.

The value of the ultimate shear, V_u corresponding to the bilinear curve is then found by ensuring that the area under the bilinear curve is equal to the area under the FEA pushover curve (equivalent energy dissipation principle). The displacement at elastic limit δ_e was found by dividing the V_u by the elastic stiffness value k_{el}. The parameters defining the bilinear force displacement response for each simulation are presented in Table 3, where $\mu = \delta_u/\delta_e$ is the displacement ductility factor, $q=(2\mu-1)^{1/2}$ is the ductility based force reduction factor and strength degradation factor, $C_{sd} =V_{\delta u}/ V_{max}$.

4.4   Comparison of FEA Result with NZSEE Predictions

The maximum shear (in-plane lateral load) capacity and the probable failure patterns (that is, the failure mode returning the lowest calculated shear capacity) of the walls were predicted using the NZSEE guidelines [22] to allow comparison with the FEA results. The results obtained from the FEA analyses are presented along with the NZSEE predictions in

Table 4. In the case of the NZSEE predictions, both fixed-fixed and fixed-free boundary conditions were considered for the piers to assess the influence of this assumption on the load capacity and the governing failure mode. The fixed-fixed assumption represents a high degree of flexural coupling of the piers by the connecting spandrel, whereas the fixed-free assumption assumes that the spandrel provides negligible flexural coupling of the piers. The effective pier height for the NZSEE predictions was taken from the base of the pier up to two-thirds of the arch radius above the base of the arch, as recommended by NZSEE for the case of deep arches such as the semi-circular arches considered in the current study.

Comparing the maximum shear capacities in Table 4, it can be seen that in general the NZSEE strength predictions agree well with the values of V_{max} obtained from the FEA simulations. For almost all of the scenarios considered, the NZSEE predictions calculated using fixed-fixed and fixed-free boundary conditions for the piers bound the FEA predicted capacity from above and below, respectively. At low pre-compression levels and slender pier configurations, the FEA predicted shear capacities are more closely matched to the NZSEE [22] predictions calculated assuming fixed-fixed boundary conditions for the piers (1-F). With increasing pre-compression level and for more squat piers, the FEA simulated shear capacities approach the NZSEE predictions assuming cantilever boundary conditions for the piers (1-C). This can be explained by the observation that at higher axial stress levels, increased damage is observed in the spandrel and the pier/spandrel connection, so that the effectiveness of the spandrel in coupling the piers is reduced and the pier behaves more as a cantilever.

5. Assessment of Effective Pier Height for Arched Openings

For a deep arched spandrel, NZSEE [22] recommends that strength calculations be based on an equivalent rectangular spandrel formed by extending the arch by one third of the radius below the apex to determine the effective depth of the spandrel. Therefore, in the comparison of the FEA results with the NZSEE, Part C-Detailed Seismic Assessment, C8: Unreinforced Masonry Buildings [22] strength predictions presented above, the effective pier height was taken as extending two-thirds of the arch radius above the base of the arch opening (C8:URM in Fig. 16a). To assess the suitability of this recommendation, the arched opening was converted to a rectangular opening and FE analyses were performed replacing the arch with additional masonry courses beneath the spandrel as shown in Fig. 16b. To assess an appropriate effective depth for the equivalent rectangular spandrel (and resulting effective height for the equivalent rectangular piers) varying numbers of additional courses (between 2 and 5) were considered.

The results from the FE analyses of walls with an arched opening and the rectangular opening with different numbers of additional masonry courses were compared according to load-displacement behaviour. The additional courses were counted from the top of the arch bricks (see Fig. 16a). Furthermore, the comparisons considered two wall geometries and two pre-compression stresses (Fig. 17). In all cases, the load-displacement response for the wall with the arched opening agreed closely with the extended rectangular opening which included an additional four masonry courses, particularly with regard to the initial displacements. It is interesting to note that the post peak decrease of the load with increasing displacement is more prominent in the case of rectangular openings. The arch opening has the arching effect, which has the capability to resist more load than the equivalent rectangular geometry.

According to the one-third / two-third radius recommendation of [22], the equivalent rectangular spandrel was at nearly three bricks extension. However, the results from the three brick extension models did not match well with the arched opening model, especially at low displacement levels. The load-displacement response for the arched opening lay between the four and five brick extension models during the linear portion of the response with closest overall match to the four bricks extension. The four bricks extension equates to an increase in spandrel depth of nearly half of the arch radius. Hence, the pier effective height for semicircular openings with this radius can be taken by extending the straight portion of the piers by half of the arch radius.

6. Masonry Compression Prism Test Model

In Section 3.3.1 it was observed that the FEA over-predicted the initial stiffness of the experimentally tested walls. To better understand the possible reasons for this observation, the masonry prism compression test which was

used to determine experimentally the elastic moduli for the masonry, the masonry units and the mortar was simulated using the FE model. The same two dimensional plane stress simplified micro-modelling strategy as used for the wall models was adopted. The seven brick high prism was modelled with top steel plates, replicating the prisms tested in the laboratory. The input material properties were the same as used for the URM wall models. A unit vertical displacement was applied at the top centre of the steel plate and the self weight of the masonry was included. First, a linear analysis was performed for the combined self-weight and unit vertical displacement. The contour of the vertical displacement is shown in Fig. 18. Following the linear analysis, non-linear analysis was conducted. In the nonlinear analysis, the self-weight was applied and kept constant in a single step. Vertical displacement was then applied by increasing, using a step size of 0.1 mm, up to a total of 4.5 mm, at which point a post peak reduction in load exceeding 20% had been achieved.

The strain was calculated by taking the displacement in between two nodes of N-170 and N-62 (Fig. 18). The nodes were selected in such a way as to span across three units and three joints. This gauge length matched that used in the experimental program. The displacement difference of the two nodes were divided by the length between the two points (gauge length) to determine the strain. The stress was calculated by dividing the force value by the bedding area of the prism (230 mm ×110 mm). Finally, the stress was plotted against strain in Fig. 19 and the modulus of elasticity was calculated by measuring the slope of a secant between ordinates corresponding to 5% and 33% of the ultimate strength of the specimens [28]. This matched identically with the approach taken to determine elastic moduli in the experimental program.

The calculated modulus of elasticity for masonry from the FEA analysis is 2460 MPa. The average value obtained from the six experimentally tested prisms was 2364 MPa. Also, the input compressive strength of the prism was 7.0 MPa (tested result) and the output maximum stress from the FEA is 7.32 MPa. Therefore, both the compressive strength and modulus of elasticity values agree well with the tested results. This is perhaps a trivial outcome, given that the input parameters used in the FEA were in fact derived from the same compression prism tests. However, this exercise does confirm that the FEA modelling approach adopted does correctly represent masonry stiffness and strength properties for compressive loading normal to the mortar bed joints. It is believed that the stiffness mismatch between the FEA simulated and experimentally tested walls relates to masonry orthotropy and the complex combination of bending and shear strains induced under the in-plane lateral loading. Despite the use of a micro modelling approach which discretely models the masonry bonding pattern, the model was not able to correctly replicate the experimentally observed wall stiffness.

7. Conclusions

The behaviour of unreinforced masonry walls with openings (pier /spandrel sub-assemblies) subjected to vertical compression, combined with in-plane lateral loading was studied using finite element micro-modelling. The FEA model was first verified against experimental test data from a series of full scale wall tests conducted by the authors, and then a parametric study was carried out. For the range of aspect ratios and pre-compression levels considered in the present study, the following observations can be summarised.

- The FEA model successfully captured the global in-plane behaviour of the tested walls and the maximum lateral strength is well matched with the experimental results. Although the crack patterns predicted by the model are not exactly in agreement with the test results, the FEA model successfully captured the expected failure modes for most of the tested walls. The exception was shear failure observed in the pier of some of the walls, this not being predicted by the FEA model.

- Maximum in-plane shear capacity increases with increasing pre-compression level and greater damage was observed in the piers and spandrel associated with the increased load levels.

- The load displacement behaviours experienced by the walls are relatively insensitive to pier aspect ratio across the range of geometries for which pier area and wall height are unchanged.

- There is no noticeable effect on the elastic stiffness with the change of the pre-compression level. However, this effect is remarkable with the change of wall geometry. The ductility values and the ultimate displacement decreased with increasing pre-compression level. However, ductility values were greater than 3.5 in all cases investigated, which is significantly greater than the code specified values for URM structures around the world.

- The maximum shear capacities of the walls obtained from FEA are comparable to the NZSEE predictions, but in some cases there is a dissimilarity in predicted failure modes.

- The effective pier height for an equivalent rectangular pier adjacent to a semi-circular arched opening can be taken up to the half height of the arch radius.

- The unidirectional compression prism model showed good agreement with the tested data. However, the FE model over-predicted the initial stiffnesses of the tested URM walls. This is believed to result from the orthotropic nature of the masonry. The orthotropy of masonry is theoretically considered in the micro modelling approach, where the bricks are modelled by continuum elements and the joints by interface elements using a combined Coulomb friction/tension cut-off/compression cap model. However, the input

for this interface model here comes from the assumptions of isotropic behaviour of masonry by applying one direction loading.

Acknowledgment

References

[1] Asteris PG., Sarhosis V., Mohebkhah A., Plevris V., Papaloizou L., Komodromos P., Lemos JV. Numerical modeling of historic masonry structures. In Handbook of research on seismic assessment and rehabilitation of historic structures IGI Global; 2015, Chapter 7, 213-256.

[2] Page AW. Finite element model for masonry. Journal of the Structural Division 1978; 104(8): 1267-85.

[3] Lourenço PB. Computational strategies for masonry structures. PhD Thesis, Delft University of Technology (TU Delft), Netherlands; 1996.

[4] Yi T., Moon FL., Leon RT., Kahn LF. Lateral load tests on a two-story unreinforced masonry building. Journal of Structural Engineering 2006; 132(5): 643-52.

[5] Nateghi FA., Alemi F. Experimental study of seismic behaviour of typical Iranian URM brick walls. In: Proceedings of the 14th World Conference on Earthquake Engineering, Beijing, China; 2008.

[6] Bothara JK., Dhakal RP. Mander JB. Seismic performance of an unreinforced masonry building: an experimental investigation. Earthquake Engineering & Structural Dynamics 2010; 39(1): 45-68.

[7] Augenti N., Parisi F., Prota A., Manfredi G. In-plane lateral response of a full-scale masonry subassemblage with and without an inorganic matrix-grid strengthening system. Journal of Composites for Construction 2011; 15(4): 578-90.

[8] Vanin A., Foraboschi P. In-plane behavior of perforated brick masonry walls. Materials and Structures 2012; 45(7): 1019-34.

[9] Knox CL., Dizhur D., and Ingham JM. Experimental cyclic testing of URM pier-spandrel substructures. Journal of Structural Engineering 2016; 143(2):04016177.

[10] Triller P., Tomaževič M., Gams M. Seismic behaviour of multistorey plain masonry shear walls with openings: An experimental study. In: Proceedings of the 16th International Brick and Block Masonry Conference, Padova, Italy; 2016.

[11] Magenes G., Fontana A. Simplified non-linear seismic analysis of masonry buildings. In: Proceedings of the 5th International Masonry Conference, London; 1998.

[12] Belmouden Y., Lestuzzi P. An equivalent frame model for seismic analysis of masonry and reinforced concrete buildings. Construction and building materials 2007; 23(1):40-53.

[13] Chen S.Y., Moon F., Yi T. A macroelement for the nonlinear analysis of in-plane unreinforced masonry piers. Engineering Structures 2008; 30(8):2242-52.

[14] Lagomarsino S., Penna A., Galasco A., Cattari S. TREMURI program: an equivalent frame model for the nonlinear seismic analysis of masonry buildings. Engineering Structures 2013; 56 :1787-99.

[15] Brencich A., Gambarotta L., Lagomarsino S. A macroelement approach to the three-dimensional seismic analysis of masonry buildings. In: Proceedings of the 11th European Conference on Earthquake Engineering, Balkema, Rotterdam; 1998.

[16] Asteris PG., Cotsovos D., Chrysostomou C., Mohebkhah A., Al-Chaar G. Mathematical micromodeling of infilled frames: state of the art. Engineering Structures 2013; 56:1905-21.

[17] Farshchi DM., Motavalli M., Schumacher A., Marefat, MS. Numerical modelling of in-plane behaviour of URM walls and an investigation into the aspect ratio, vertical and horizontal post-tensioning and head joint as a parametric study. Archives of Civil and Mechanical Engineering 2009; 9(1):5-27.

[18] Betti M., Galano L., Vignoli A. Comparative analysis on the seismic behaviour of unreinforced masonry buildings with flexible diaphragms. Engineering Structures 2014; 61:195-208.

[19] Allen C., Masia MJ., Page AW., Griffith MC., Ingham JM. Nonlinear finite element modelling of unreinforced masonry walls with openings subjected to in-plane shear. In: Proceedings of the 13th Canadian Masonry Symposium, Halifax, Canada; 2017.

[20] Zhang S., Yang D., Sheng Y., Garrity SW., Xu L. Numerical modelling of FRP-reinforced masonry walls under in-plane seismic loading. Construction and Building Materials 2017; 134: 649-63.

[21] DIANA FEA. DIANA finite element analysis user's manual release 10.0. Delft, The Netherlands; 2017.

[22] NZSEE. The seismic assessment of Existing buildings, Technical guidelines for engineering assessments. section C8-Seismic assessment of unreinforced masonry buildings, New Zealand Society for Earthquake Engineering, New Zealand; 2017.

[23] Howlader MK, Masia MJ, Griffith MC. Cyclic in-plane testing of simulated Australian historical perforated URM walls. In: Proceedings of the 13th North American Masonry conference, Salt Lake City; 2019.

[24] Petersen RB., Masia MJ., Seracino R. In-plane shear behavior of masonry panels strengthened with NSM CFRP strips. I: Experimental investigation. Journal of Composites for Construction 2010; 14(6), 754-63.

[25] Konthesingha C. Earthquake protection of masonry shear walls using Fibre Reinforced Polymer strengthening. PhD Thesis, School of Engineering, The University of Newcastle, Australia; 2012.

[26] Lourenço PB., Rots JG. Multisurface interface model for analysis of masonry structures. Journal of Engineering Mechanics 1997; 123(7): 660-68.

[27] Van Zijl, GP. Modeling masonry shear-compression: Role of dilatancy highlighted. Journal of Engineering Mechanics 2004; 130(11):1289-96.

[28] Drysdale RG., Hamid AA., Baker LR. Masonry structures: behavior and design. Prentice Hall, Prentice Hall.0135620260; 1994.

[29] Standard Australia. Masonry Structures: Appendix C- Method of test for compressive strength. AS3700, Standards Australia Limited, Australia; 2018.

[30] European Standard. Methods of test for masonry-Part 3: Determination of initial shear strength. Design code EN1052-3, European committee of standerization, Brussels, Belgium; 2002.

[31] Standard Australia. Masonry Structures: Appendix D- Method of test for flexure strength. AS3700, Standards Australia Limited, Australia; 2018.

[32] Standard Australia. Masonry units, segmental pavers and flags—Methods of test, Method 15: Determining lateral modulus of rupture. AS/NZS 4456.15, Standards Australia Limited and Standards New Zealand, Australia and New Zealand; 2003.

[33] Lourenço PB. Structural masonry analysis: Recent developments and prospects. In: Proceedings of the 14th International Brick and Block Masonry Conference, Sydney, Australia; 2008.

[34] Lourenço PB. A user/programmer guide for the micromodeling of masonry structures, TU-DELFT report no. 03.21.1.31.35, TNO Building and Construction Research, Computational Mechanics, Delft University of Technology & University of Minho; 1996.

[35] Petersen RB. In-plane shear behaviour of unreinforced masonry panels strengthened with fibre reinforced polymer strips. PhD Thesis, School of Engineering, The University of Newcastle, Australia; 2009.

[36] Masia MJ., Han Y., Player CJ., Correa MRS., Page AW. Torsion shear test for mortar joints in masonry: Preliminary experimental results. In: Proceedings of the 10th North American Masonry Conference, St Louis, Missouri, U.S.A; 2007.

[37] Knox CL. Assessment of perforated unreinforced masonry walls responding in-plane. PhD Thesis, Department of Civil and Environmental Engineering, The University of Auckland, New Zealand; 2012.

[38] Howlader MK., Masia MJ., Griffith MC., Ingham JM., Jordan JW. Characterisation of heritage masonry construction in NSW - State Heritage Register. In: Proceedings of the Australian Earthquake Engineering Society conference, Melbourne, Australia; 2016.

[39] Frumento S., Magenes G., Morandi P., Calvi GM. Interpretation of experimental shear tests on clay brick masonry walls and evaluation of q-factors for seismic design, Iuss Press Pavia.8861980341; 2009.

[40] Magenes G., Morandi P., Penna A. Test results on the behavior of masonry under static cyclic in-plane lateral loads, ESECMaSE project, Department of Structural Mechanics, University of Pavia, Italy; 2008.

[41] Van der Pluijm R. Non-linear behaviour of masonry under tension. HERON, 1997; 42(1), 25-54.

[42] Howlader MK., Masia, MJ., Griffith, MC. Prediction of in-plane shear capacity of perforated URM walls: nonlinear finite element modeling compared with the NZSEE formula. In: Proceedings of the *10th International Masonry Conference*, Milan, Italy; 2018.

List of Figures
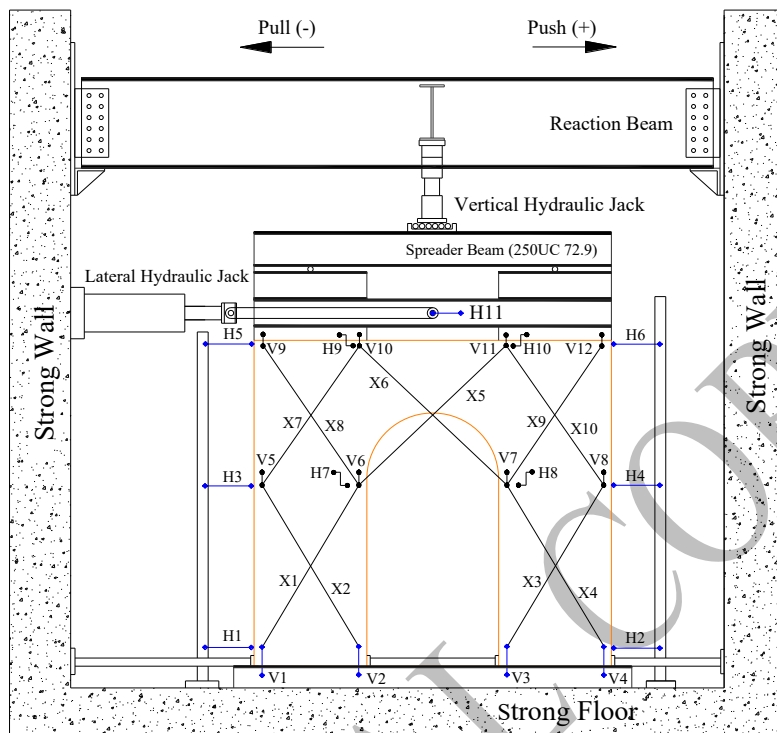
Fig. 1: Elevation of the wall test setup and instrumentation (H, V, X denotes horizontal, vertical and diagonal respectively).
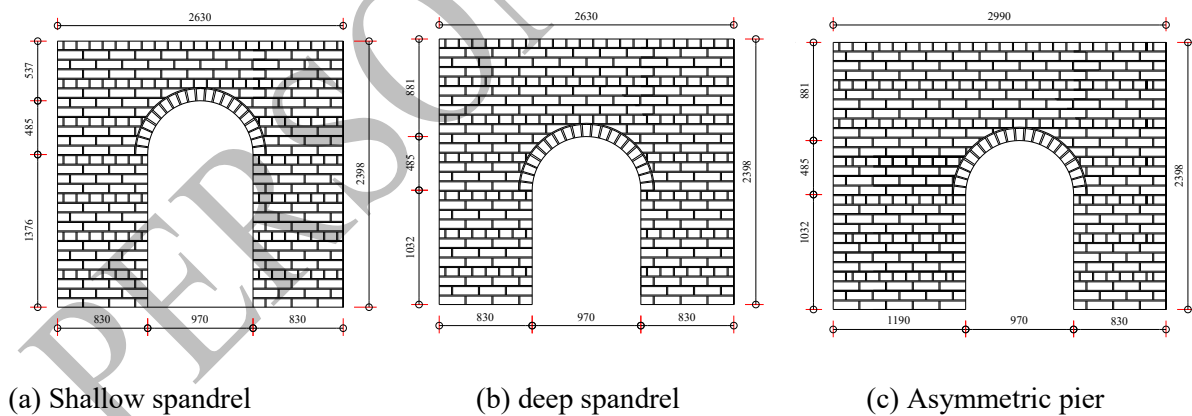
(a) Shallow spandrel   (b) deep spandrel   (c) Asymmetric pier

Fig. 2: Tested wall specimens (all dimensions are in mm).
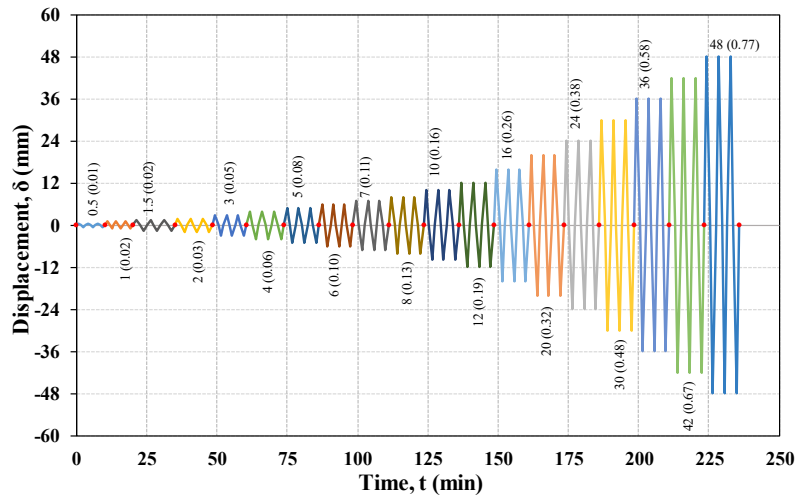
Fig. 3: Applied displacement time history for test specimens.

(a) masonry assemblage

(b) meshing in FE model
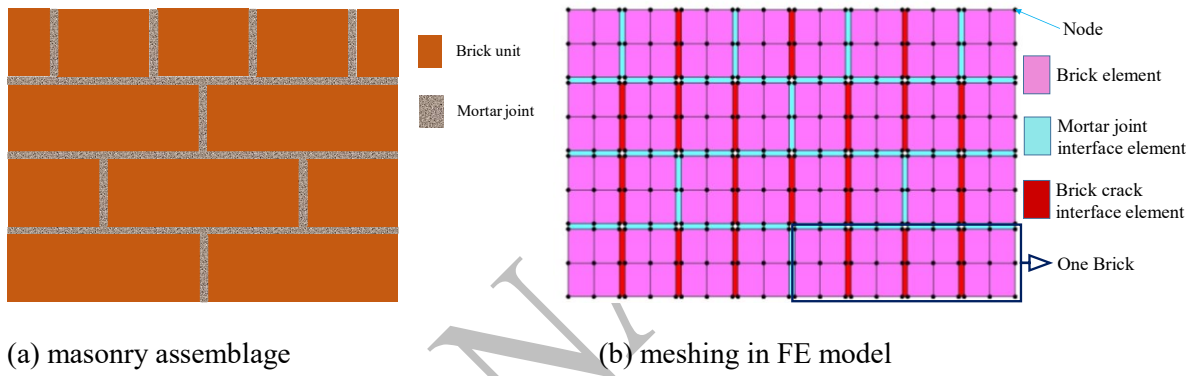
Fig. 4: Simplified micro-modelling approach used to model the walls.
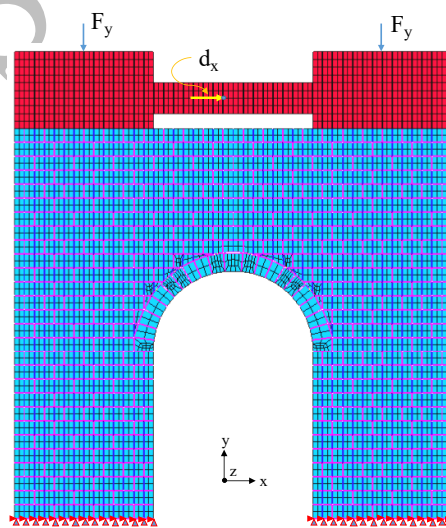
Fig. 5: Illustration of FE modelling for deep spandrel wall.
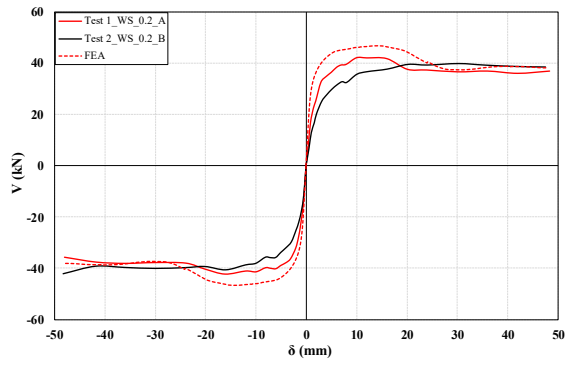
(a) WS_0.2
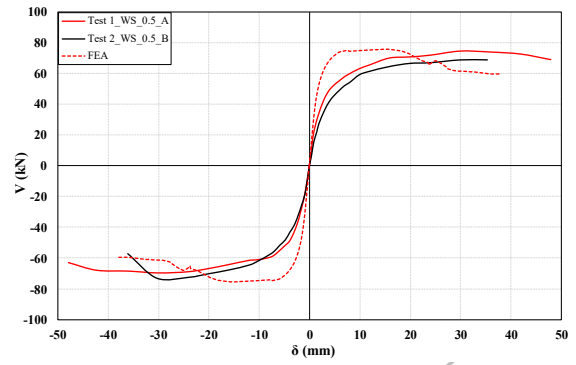
(b) WS_0.5
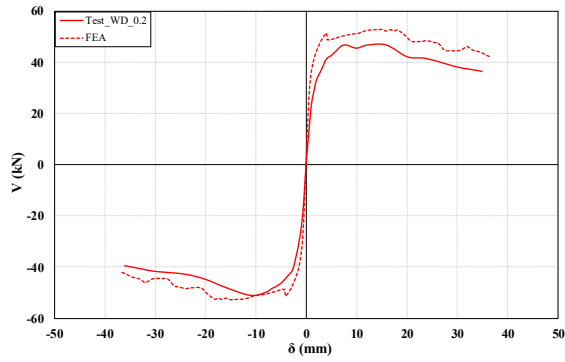
(c) WD_0.2
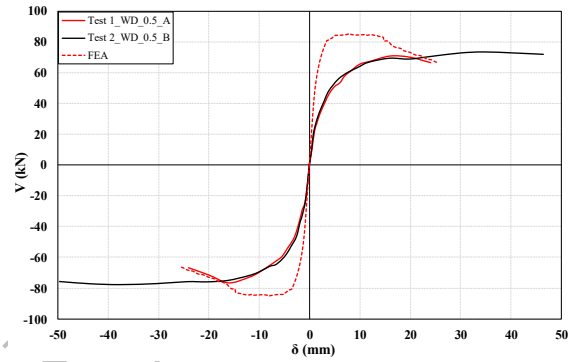
(d) WD_0.5
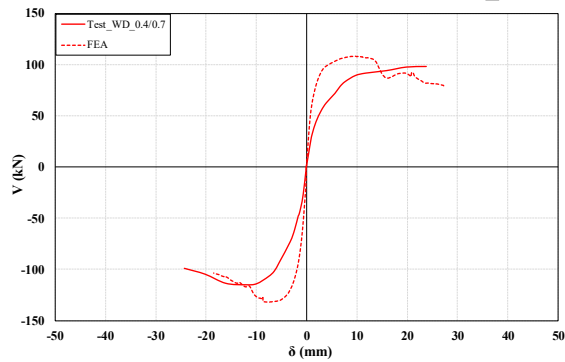
(e) WD_0.4/0.7

Fig. 6: Lateral load-displacement behaviour of walls.
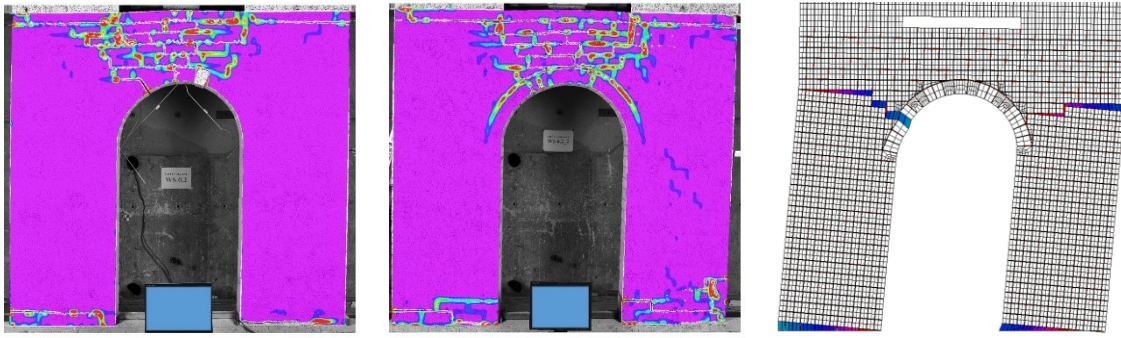
(a) Test-WS_0.2_A   (b) Test-WS_0.2_B   (c) FEA-WS_0.2

Fig. 7: Crack patterns at ultimate state of wall WS_0.2.
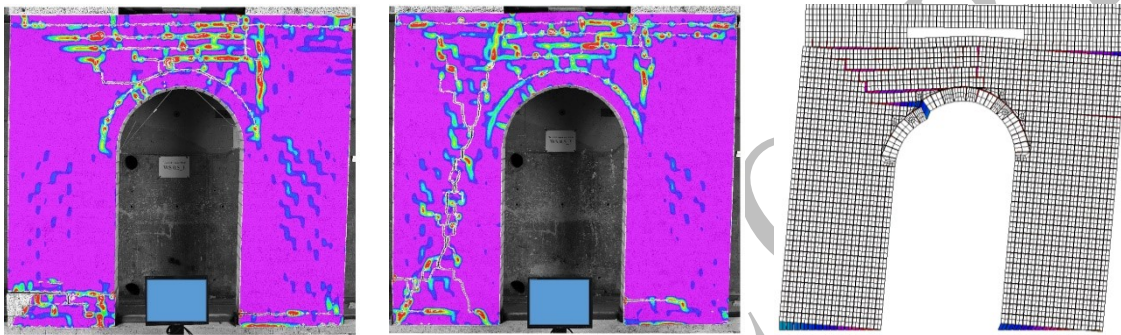
(a) Test-WS_0.5_A   (b) Test-WS_0.5_B   (c) FEA-WS_0.5

Fig. 8: Crack patterns at ultimate state of wall WS_0.5.
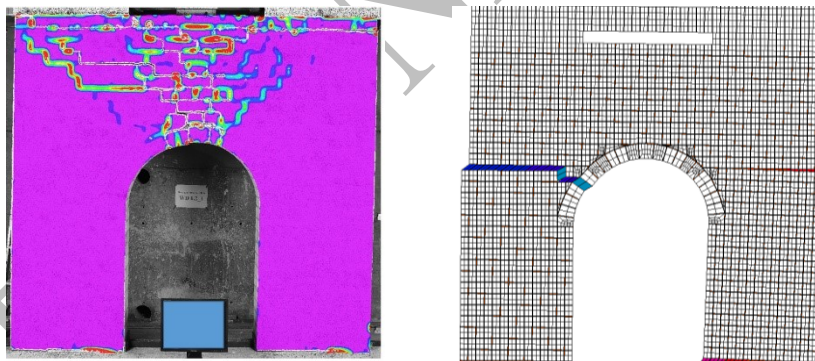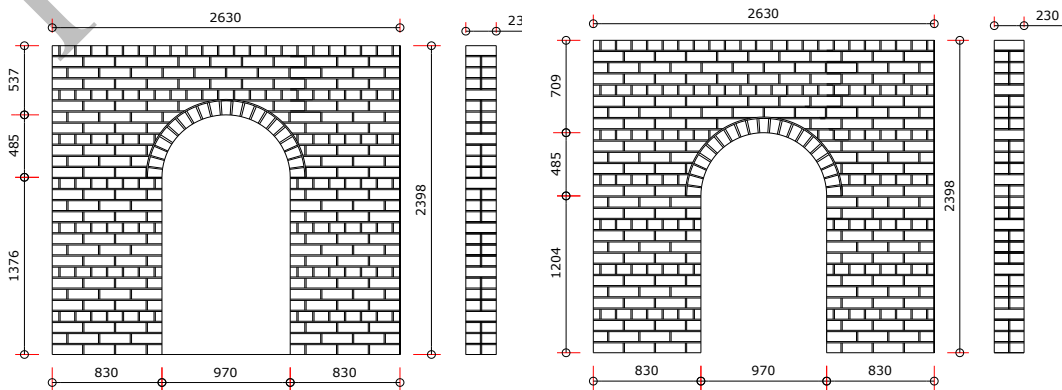

(a) Test-WD_0.2   (b) FEA-WD_0.2

Fig. 9: Crack patterns at ultimate state of wall WD_0.2.
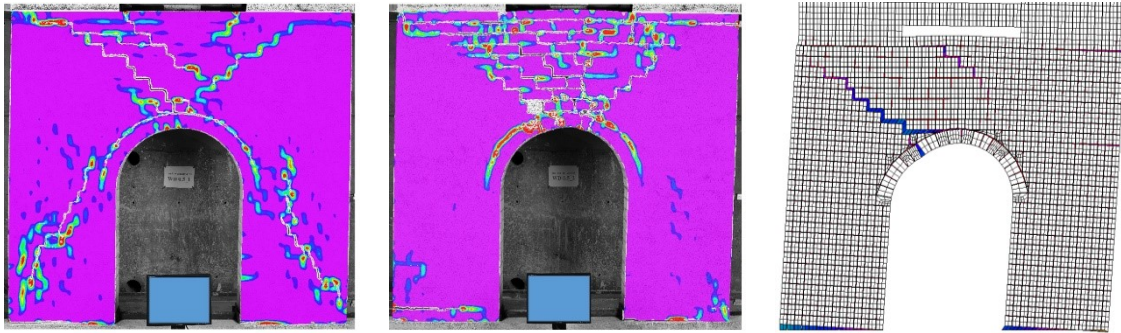
(a) Test-WD_0.5_A   (b) Test-WD_0.5_B   (c) FEA-WD_0.5

Fig. 10: Crack patterns at ultimate state of wall WD_0.5.
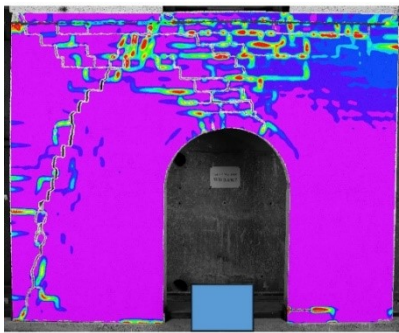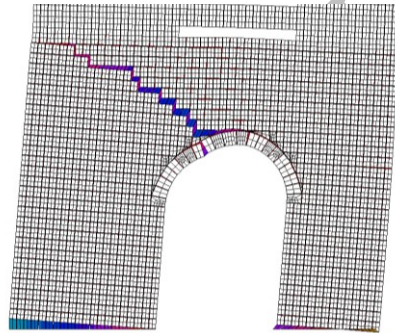
(a) Test-WD_0.4/0.7 (+)   (b) FEA-WD_0.4/0.7 (+)
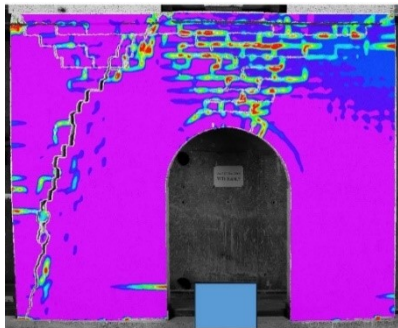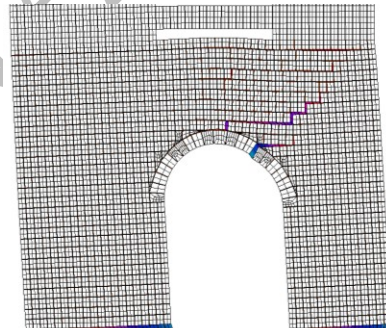
(c) Test-WD_0.4/0.7 (-)   (d) FEA-WD_0.4/0.7 (-)

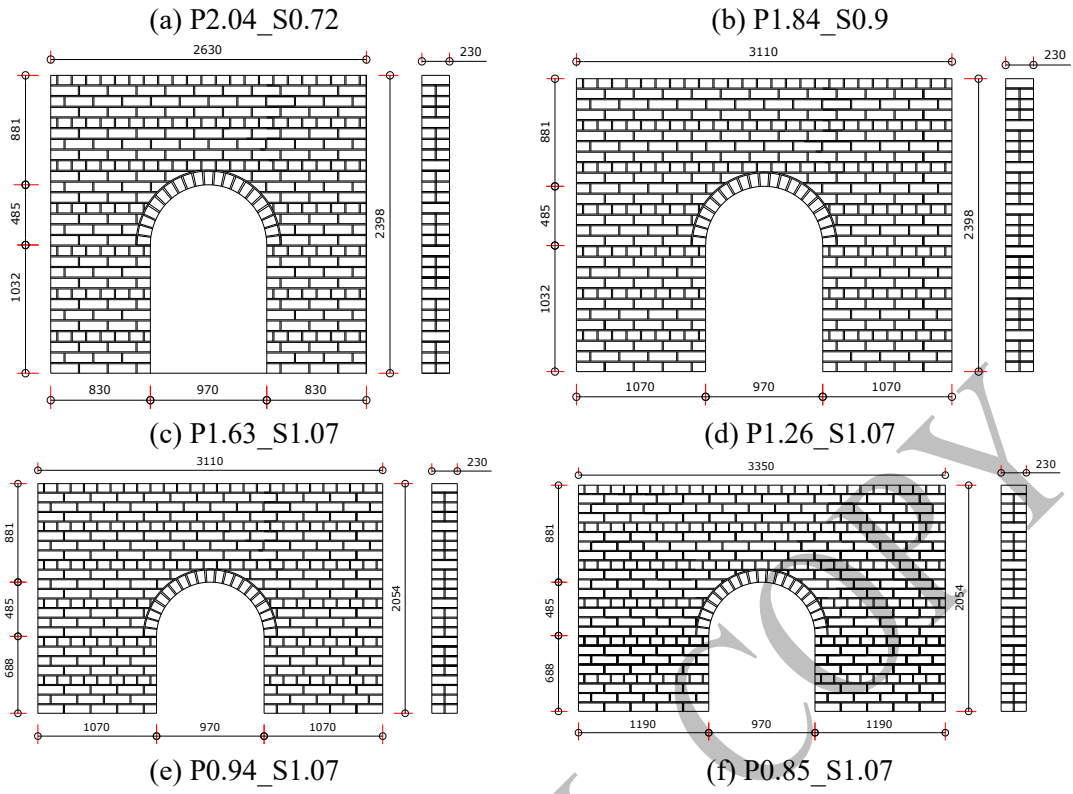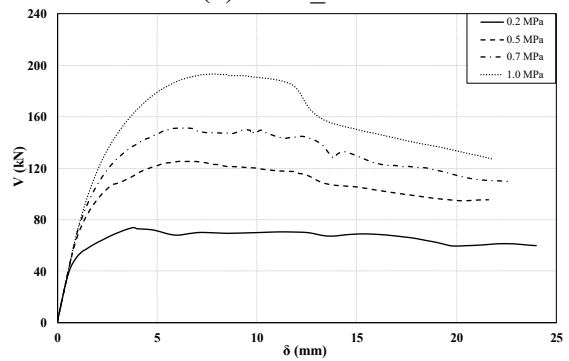Fig. 11: Crack patterns at ultimate state of wall WD_0.4/0.7.

(a) P2.04_S0.72   (b) P1.84_S0.9

(c) P1.63_S1.07   (d) P1.26_S1.07
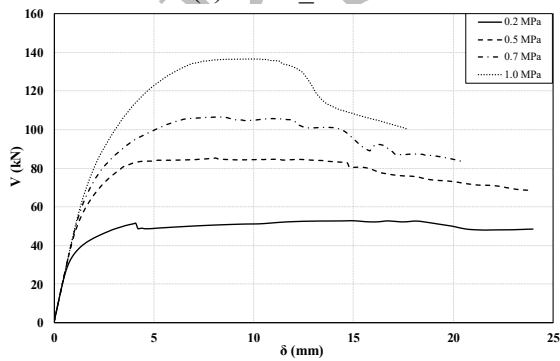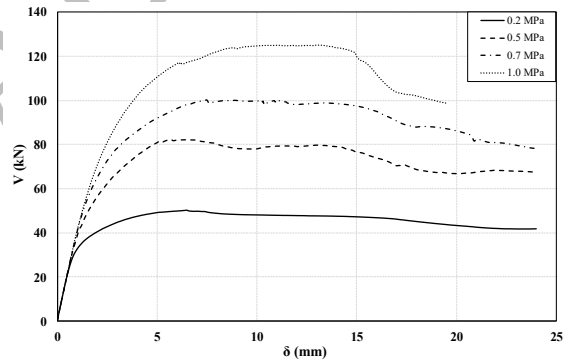
(e) P0.94_S1.07   (f) P0.85_S1.07

Fig. 12: Geometries chosen for parametric study (all dimensions are in mm).

(a) P2.04_S0.72   (b) P1.84_S0.9
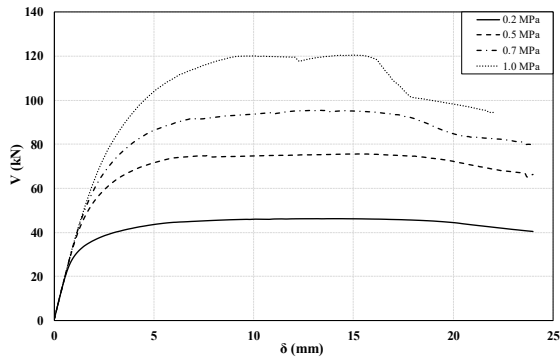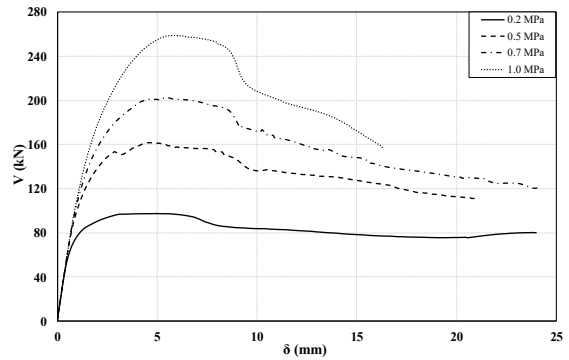
(c) P1.63_S1.07   (d) P1.26_S1.07
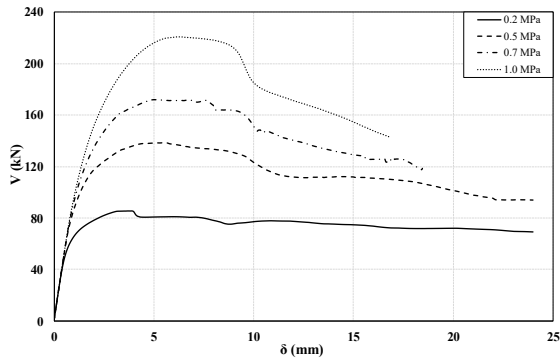
(e) P0.94_S1.07   (f) P0.85_S1.07

Fig. 13: Load displacement response for different geometries with the variation of axial pre-compression stresses.
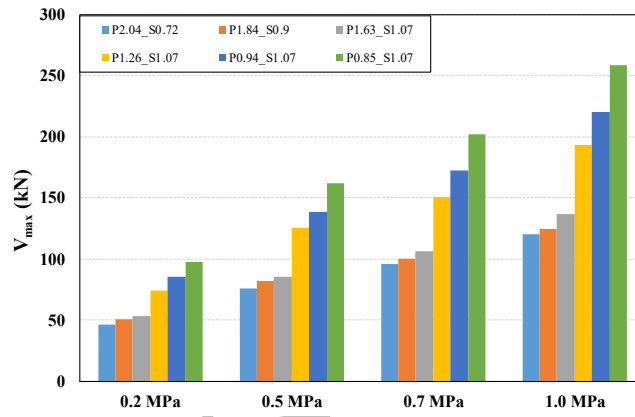

Fig. 14: Maximum shear strength for different configurations.
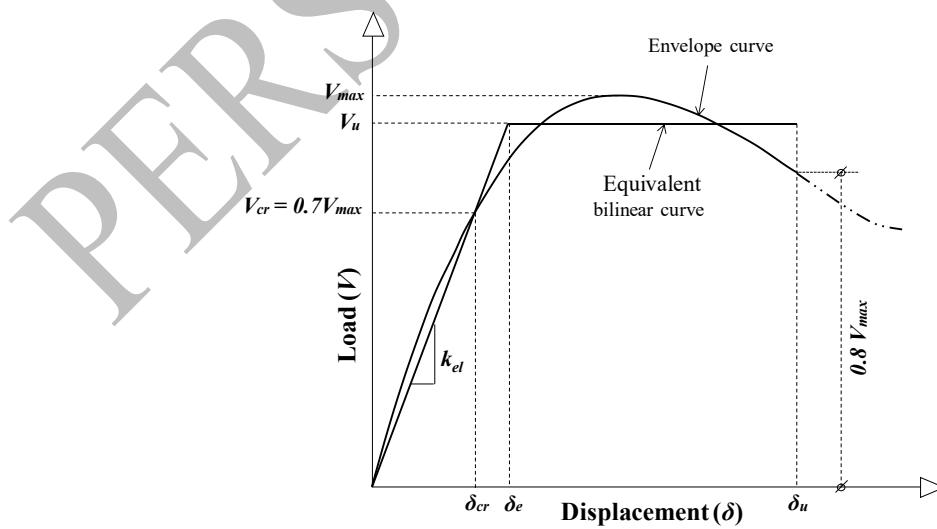
Fig. 15: Bilinear idealisation of the load displacement curve (adapted from [40])
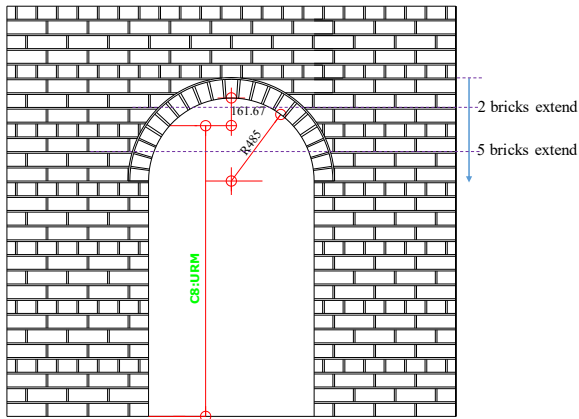
(a) Arched opening wall
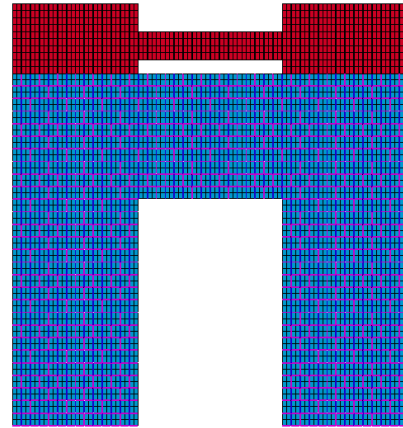
(b) equivalent rectangle FE model (extended by 5 bricks)

Fig. 16: Illustration of brick layer extensions to make equivalent rectangular openings.
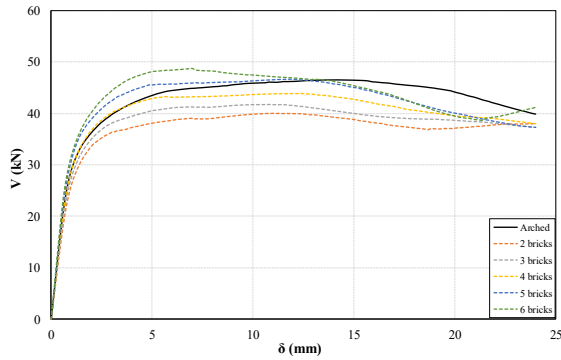
(a) shallow spandrel-0.2 MPa
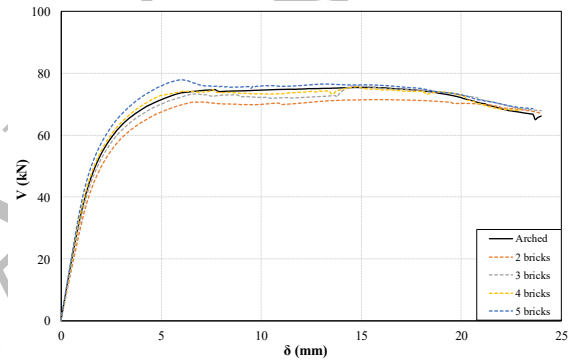
(b) shallow spandrel-0.5 MPa
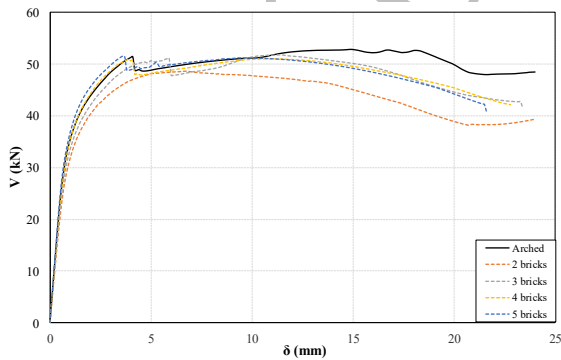
(c) deep spandrel-0.2 MPa

(d) deep spandrel-0.5 MPa

Fig. 17: Comparison of load-displacement behaviour for arched opening with the different depth of rectangular opening.

Fig. 18: Vertical displacement contour of the masonry prism.

Fig. 19: Stress-strain plot for masonry prism FEA simulation.

List of Tables

Table 1: Material properties used in FE modelling of walls.

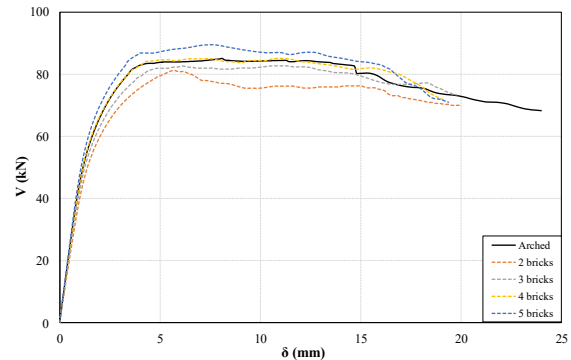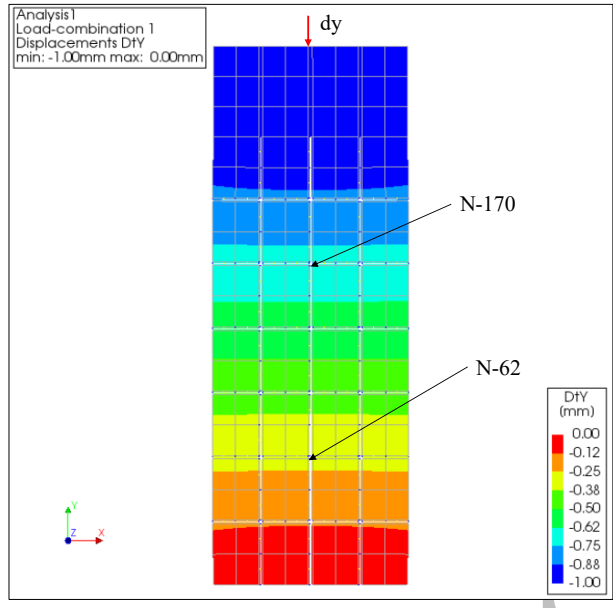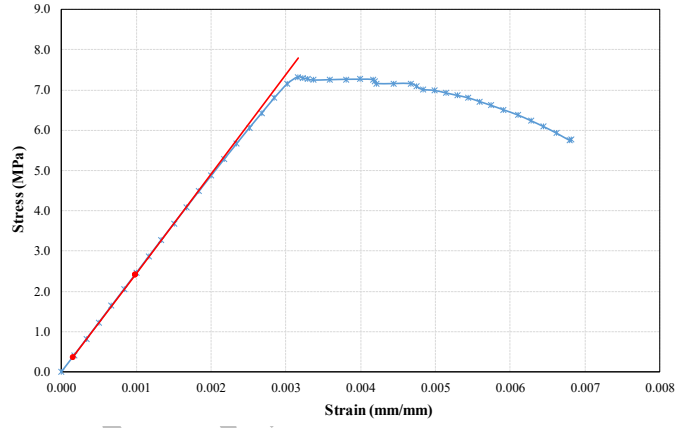| Material	Property	Value	Unit	Source of data
Brick	Young's modulus (E_b)	2502	MPa	Compression test
	Poisson's ratio (v)	0.2	--	Assumed
	Tensile strength (f_{bt})	0.71	MPa	Modulus of rupture test
	Tensile fracture energy (G^I_f)	0.025	N/mm	[33]
Steel	Young's modulus (E_{st})	200	GPa	Assumed
	Poisson's ratio (v)	0.3	--	Assumed
Joint	Normal stiffness (k_n)	523	N/mm³	Compression test [26]
	Shear stiffness (k_s)	218	N/mm³	Compression test [26]
	Tensile strength (f_{jt})	0.10	MPa	Bond wrench test
	Tensile fracture energy (G^I_f)	0.012	N/mm	[34]
	Cohesion (c_0)	0.15	--	Triplet test
	Initial friction coefficient ($tan\varphi_i$)	0.74	--	Triplet test
	Initial dilatancy coefficient ($tan\psi_0$)	0.50	--	[35]
	Residual friction coefficient ($tan\varphi_r$)	0.56	--	[36]
	Confined normal stress (σ_u)	-0.75	MPa	[35]
	Exponential degradation coefficient (δ)	1.8	--	[35]
	Masonry compressive strength (f_c)	7.0	MPa	Compression test
	Compressive fracture energy (G_c)	11.2	N/mm	Compression test
	Shear traction control factor (C_s)	9.0	--	[34]
	Equivalent plastic relative displacement (κ_p)	0.0128	mm	Compression test
	Fracture energy factor (a) (G^{II}_f)	-0.80	--	[35]
	Fracture energy factor (b) (G^{II}_f)	0.05	--	[35]

Table 2: FEA prediction and experimental maximum loads of URM walls

Wall Id	Test (kN)	FE model (kN)	% Error
WS_0.2	41.5	46.6	12.3
WS_0.5	71.6	75.6	5.6
WD_0.2	48.9	52.8	7.9
WD_0.5	74.6	85.2	14.2
WD_0.4/0.7 (+)	98.3	107.9	9.8
WD_0.4/0.7 (-)	114.9	128.2	11.6

Table 3: Summary of the bilinear properties of FE analysed URM walls.

Wall ID	σ (MPa)	k_{el} (kN/mm)	V_{max} (kN)	V_u (kN)	V_u/V_{max} (--)	δ_u (mm)	δ_e (mm)	μ (--)	q (--)	C_{sd} (--)
P2.04_S0.72	0.2	24.2	46.2	44.5	0.96	24.00	1.84	13.0	5.0	0.87
	0.5	27.4	75.6	72.9	0.96	24.00	2.66	9.0	4.1	0.88
	0.7	26.8	93.4	90.2	0.95	24.00	3.36	7.1	3.6	0.85
	1.0	26.9	120.3	113.1	0.94	20.98	4.21	5.0	3.0	0.80
P1.84_S0.90	0.2	28.3	50.2	46.2	0.92	24.00	1.63	14.7	5.3	0.83
	0.5	27.2	82.3	75.2	0.91	24.00	2.77	8.7	4.0	0.82
	0.7	30.2	100.2	93.6	0.93	22.68	3.09	7.3	3.7	0.80
	1.0	30.2	124.9	118.1	0.94	18.87	3.91	4.8	2.9	0.80
P1.63_S1.07	0.2	32.7	52.8	50.5	0.96	24.00	1.54	15.6	5.5	0.92
	0.5	37.3	85.2	79.4	0.93	24.00	2.13	11.3	4.6	0.80
	0.7	36.0	106.5	98.5	0.92	19.70	2.73	7.2	3.7	0.80
	1.0	34.2	136.6	130.2	0.95	14.67	3.81	3.9	2.6	0.80
P1.26_S1.07	0.2	46.3	74.0	67.3	0.91	24.00	1.45	16.5	5.7	0.81
	0.5	53.5	125.3	115.7	0.92	17.05	2.16	7.9	3.8	0.80
	0.7	54.5	151.1	139.8	0.93	17.78	2.56	6.9	3.6	0.80
	1.0	53.0	193.0	183.6	0.95	13.85	3.46	4.0	2.6	0.80
P0.94_S1.07	0.2	76.6	85.4	76.9	0.90	20.54	1.00	20.5	6.3	0.84
	0.5	78.7	138.3	124.3	0.90	16.10	1.58	10.2	4.4	0.80
	0.7	76.3	172.2	161.4	0.94	12.62	2.12	6.0	3.3	0.80
	1.0	74.2	220.5	207.8	0.95	10.95	2.83	3.9	2.6	0.80
P0.85_S1.07	0.2	90.7	97.2	87.9	0.90	15.41	0.97	15.9	5.6	0.80
	0.5	89.9	161.8	146.6	0.91	14.34	1.63	8.8	4.1	0.80
	0.7	89.7	202.4	187.6	0.93	11.96	2.09	5.7	3.2	0.80
	1.0	87.8	258.5	244.6	0.95	10.15	2.78	3.7	2.5	0.80

Table 4: Maximum load capacity and failure patterns from FEA and NZSEE 2017.

Wall ID	σ (MPa)	V_{max} (kN)			Failure Mechanism			
					FEA		1-F	1-C
		FEA	1-F	1-C	P_i	S_p	P_i	P_i
P2.04_S0.72	0.2	47	39	22	F	S	F	F
	0.5	76	88	46	F	M	F	F
	0.7	93	116	60	F	M	F	F
	1.0	121	151	77	F	M	F	F
P1.84_S0.90	0.2	50	44	24	F	S	F	F
	0.5	82	98	51	F	M	F	F
	0.7	100	129	67	F	M	F	F
	1.0	125	168	86	F	M	F	F
P1.63_S1.07	0.2	53	49	28	F	S	F	F
	0.5	85	111	58	F	M	F	F
	0.7	107	145	75	F	M	F	F
	1.0	137	190	97	F	M	F	F
P1.26_S1.07	0.2	74	82	45	F	N	F	F
	0.5	125	183	96	F	M	F	F
	0.7	151	241	125	F	M	F	F
	1.0	193	314	161	F	M	F	F
P0.94_S1.07	0.2	85	108	59	F	N	F	F
	0.5	138	193	128	F	M	S	F
	0.7	172	243	166	F	M	S	F
	1.0	221	310	215	F	M	S	F
P0.85_S1.07	0.2	97	129	73	F	N	S	F
	0.5	162	214	158	F	M	S	F
	0.7	202	270	205	F	M	S	F
	1.0	259	355	266	F	M	S	F

1-F and 1-C denote NZSEE (2017) predictions with fixed-fixed and cantilever (fixed-free) boundary conditions respectively. P_i denotes pier and S_p denotes spandrel.

For failure mechanism: F denotes flexure, S for shear (sliding through horizontal joints and/or stair stepped diagonal crack), N indicates no failure and M denotes mixed shear and flexure failure.